

Quantum process tomography of two-qubit controlled-Z and controlled-NOT gates using superconducting phase qubits

T. Yamamoto,^{1,2} M. Neeley,¹ E. Lucero,¹ R. C. Bialczak,¹ J. Kelly,¹ M. Lenander,¹ Matteo Mariantoni,¹ A. D. O'Connell,¹ D. Sank,¹ H. Wang,¹ M. Weides,¹ J. Wenner,¹ Y. Yin,¹ A. N. Cleland,^{1,*} and John M. Martinis^{1,†}

¹Department of Physics, University of California, Santa Barbara, California 93106, USA

²Green Innovation Research Laboratories, NEC Corporation, Tsukuba, Ibaraki 305-8501, Japan

(Received 19 October 2010; published 9 November 2010)

We experimentally demonstrate quantum process tomography of controlled-Z and controlled-NOT gates using capacitively coupled superconducting phase qubits. These gates are realized by using the $|2\rangle$ state of the phase qubit. We obtain a process fidelity of 0.70 for the controlled phase and 0.56 for the controlled-NOT gate, with the loss of fidelity mostly due to single-qubit decoherence. The controlled-Z gate is also used to demonstrate a two-qubit Deutsch-Jozsa algorithm with a single function query.

DOI: [10.1103/PhysRevB.82.184515](https://doi.org/10.1103/PhysRevB.82.184515)

PACS number(s): 03.67.Lx, 03.67.Ac, 85.25.Cp

I. INTRODUCTION

Quantum computation and quantum communication rely on excellent control of the underlying quantum system.¹ Reasonable control has been achieved with a variety of quantum systems with superconducting qubits emerging as one of the most promising candidates.² Recent experiments using superconducting architectures include demonstrations of quantum algorithms using two qubits³ and the entanglement of three qubits.^{4,5} A key element in these experiments is a two-qubit entangling gate, such as the \sqrt{i} SWAP (Ref. 4) and the controlled-Z (CZ) gates.^{3,5} Because the CZ gate is simple to implement, has high fidelity and can readily generate controlled-NOT (CNOT) logic,⁶ it likely will be an important component in more complex algorithms such as quantum error correction. At present, however, the CZ gate functionality has only been directly tested for a subset of the possible input states.

In this paper, we demonstrate the operation of a CZ gate in superconducting phase qubits and fully characterize this gate as well as a CNOT gate using quantum process tomography (QPT). We additionally use the CZ gate to perform the Deutsch-Jozsa algorithm,³ here with a single-shot evaluation of the function. The use of QPT provides a more complete gate evaluation than, for example, measuring the truth table for the corresponding CNOT gate,^{7,8} as it verifies that the gate will properly transform any possible input state. QPT for two- or three-qubit gates has been reported in NMR,⁹ optics,¹⁰⁻¹² and in ion traps.^{13,14} In solid-state systems, QPT has been implemented for the \sqrt{i} SWAP gate with the phase qubit.¹⁵

II. EXPERIMENT

The electrical circuit for the device is shown in Fig. 1, comprising two superconducting phase qubits A and B, coupled by a fixed capacitance C_c . Each qubit is a superconducting loop interrupted by a capacitively shunted Josephson junction, and its parallel loop inductance produce a nonlinear potential as a function of the phase difference across the junction. Combined with the kinetic energy originating from

the shunting capacitance, unequally spaced quantized energy levels appear in the cubic potential. The two lowest levels are used for the qubit states $|0\rangle$ and $|1\rangle$ with a transition frequency f_{10}^A (f_{10}^B) that can be controlled by an external magnetic flux Φ_{ex}^A (Φ_{ex}^B) applied to the loop. The third energy level $|2\rangle$ is used as an auxiliary state to realize the CZ gate, as discussed below.

The operation of a similar device has been reported previously.^{15,16} The state of each qubit is controlled by applying a rectangular-shaped current pulse (Z pulse) or a Gaussian-shaped microwave pulse (X, Y pulse) to its bias coil. For an X or Y pulse, we simultaneously apply the derivative of the pulse to the quadrature (90° phase shifted) drive to reduce both unwanted excitation of the $|2\rangle$ state and phase error due to ac Stark effect;¹⁷ the derivative scaling factor is determined from the nonlinearity of each qubit.¹⁸ This procedure enables us to use a Gaussian pulse with a full width at half maximum of 10 ns while maintaining accurate qubit control¹⁹ in spite of a rather weak qubit nonlinearity (~ 100 MHz). Each qubit state is read out individually in a single-shot manner by injecting a large magnitude Z pulse and then measuring the qubit flux with a superconducting quantum interference device (SQUID).

The device was fabricated using a photolithographic process with Al films, AlO_x tunnel junctions, and a-Si:H dielectric for the shunt capacitors and wiring crossovers, all on a sapphire substrate. The device was mounted in a superconducting aluminum sample holder and cooled in a dilution refrigerator to ~ 25 mK.

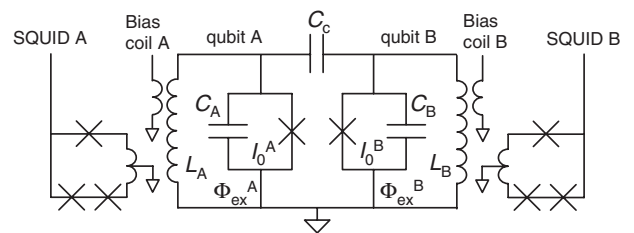


FIG. 1. Circuit diagram for the experimental device, showing two flux-biased phase qubits coupled by a fixed capacitance C_c . A bias coil and readout SQUID are coupled to each qubit. The design parameters of the circuit are $I_0^A = I_0^B = 2 \mu\text{A}$, $C_A = C_B = 1 \text{ pF}$, $L_A = L_B = 720 \text{ pH}$, and $C_c = 2 \text{ fF}$.

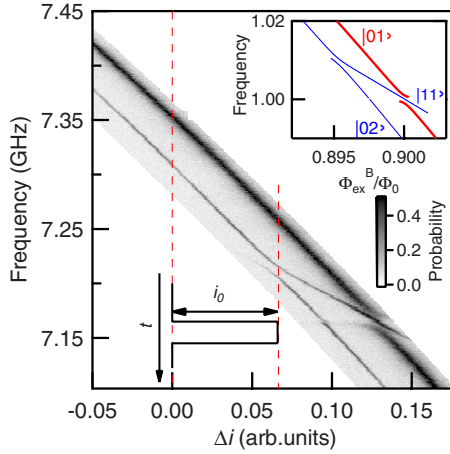


FIG. 2. (Color online) High-power spectroscopy for qubit B. The escape probability (gray scale) is plotted versus microwave frequency and the Z-pulse amplitude Δi . The single-photon $|0\rangle \rightarrow |1\rangle$ and two-photon $|0\rangle \rightarrow |2\rangle$ transitions are visible, along with two avoided-level crossings. The upper inset shows the calculated states and eigenenergies with the thick (thin) lines representing single (two) photon excitations. The lower inset illustrates the Z-pulse amplitude i_0 for the CZ gate operation.

In the present experiment, the two qubits were biased so that $f_{10}^A = 7.16$ GHz and $f_{10}^B = 7.36$ GHz when no Z pulse was applied. The relaxation times (T_1) were measured to be 510 ns and 500 ns for qubit A and B, respectively. The dephasing times determined from a Ramsey interference experiment (T_2^{Ramsey}), which showed Gaussian decay proportional to $\exp[-(t/T_2^{\text{Ramsey}})^2]$ due to $1/f$ flux noise,²⁰ were 200 ns and 230 ns, respectively.

III. RESULTS AND DISCUSSION

A. Spectroscopy

Figure 2 shows the high-power spectroscopy for qubit B, which is used to guide formation of the CZ gate. We plot the escape probability of qubit B in gray scale as a function of the amplitude Δi of a 2 μ s long Z pulse (horizontal axis) and the frequency of a microwave X pulse (vertical axis) of the same length. Both pulses were applied simultaneously to qubit B, followed by the Z pulse for the readout. In this way, we can probe the change in the resonance frequency f_{10}^B as a function of detuning Δi . In addition to the main resonance line corresponding to f_{10}^B , somewhat broadened because of the large amplitude of the microwave pulse ($\Delta\Phi_{\text{ex}}^B \sim 10\mu\Phi_0$), a sharper line is observed on the low-frequency side of the main resonance; this corresponds to the two-photon excitation from the $|0\rangle$ to the $|2\rangle$ state.²¹ The vertical distance between the main and two-photon lines is 1/2 the qubit nonlinearity $\Delta f = f_{10} - f_{21}$, yielding $\Delta f = 114$ MHz for qubit A (data not shown) and 87 MHz for qubit B.

We observe an avoided-level crossing in the main resonance at $\Delta i \approx 0.13$ when the two-qubit frequencies overlap $f_{10}^B = f_{10}^A$. Here, the degeneracy of the $|AB\rangle = |10\rangle$ and $|01\rangle$ states produces a splitting with size 14.2 ± 0.2 MHz, deter-

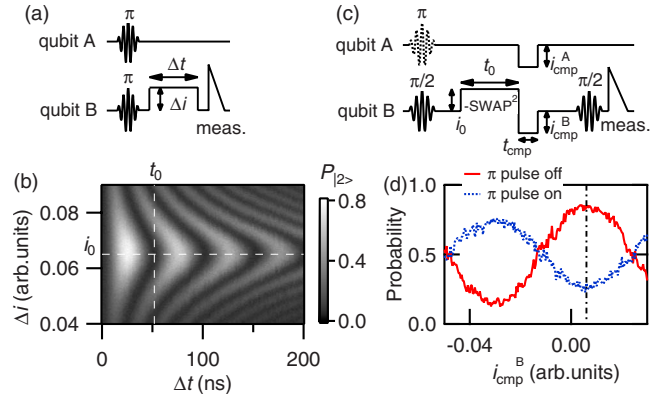


FIG. 3. (Color online) (a) Operation sequence for (b), the state evolution between $|11\rangle$ and $|02\rangle$ states. (b) Plot of $|2\rangle$ state probability of qubit B versus Z-pulse time Δt and Z-pulse amplitude Δi . The dashed lines correspond to the optimal setting for the CZ gate. (c) Operation sequence for (d), demonstration of the CZ gate. (d) Plot of $|1\rangle$ state probability of qubit B as a function of i_{cmp}^B (i_{cmp}^A is fixed as 3×10^{-4}). The (red) solid and (blue) dashed curves are for qubit A initialized to the $|0\rangle$ and $|1\rangle$ states, respectively. The vertical dotted-dashed line indicates the value of i_{cmp}^B for the CZ gate.

mined from a fit to the data, consistent with the designed capacitance C_c . The avoided crossing for the two-photon line at $\Delta i \approx 0.066$ gives a splitting of 9.7 ± 0.2 MHz, about $\sqrt{2}/2$ times as large as the main resonance, as expected from a $|11\rangle$ and $|02\rangle$ interaction. The slope of the resonance between the two crossings is 1/2 that of f_{10}^B , as expected for the $|11\rangle$ state.

Our interpretation of the spectroscopy is validated by a numerical calculation. Using three states for each qubit and the qubit design parameters, we calculate from the resulting 9×9 Hamiltonian^{22,23} the energies for the coupled eigenstates. The energy bands, normalized to f_{01}^A , are plotted versus the flux bias for qubit B in the upper inset of Fig. 2. Here, a band is plotted only when its transition matrix element from the ground state is above a threshold, to simulate the appearance of the transition in the spectroscopic measurement. The details of the calculation are described in Appendix A. The (red) thick lines correspond to the $|01\rangle$ and $|10\rangle$ states, whereas the (blue) thin lines represent half of the excitation energy of the $|11\rangle$ and $|02\rangle$ states. The overall structure agrees well with the experimental data.

B. Bring up of controlled-Z gate

As proposed theoretically by Strauch *et al.*,²⁴ the avoided crossing due to the degeneracy of the $|11\rangle$ and $|02\rangle$ states can be used to construct a CZ gate, whose action produces no change in state except for $|11\rangle \rightarrow -|11\rangle$. By applying a nonadiabatic Z pulse, the $|11\rangle$ and $|02\rangle$ states become degenerate (see lower inset of Fig. 2). Initially in the $|11\rangle$ state, the system evolves as an i SWAP interaction, giving $|\Psi(t)\rangle = \cos(\gamma\Delta t/\hbar)|11\rangle + i \sin(\gamma\Delta t/\hbar)|02\rangle$, where 2γ is the splitting energy of the avoided crossing and Δt the duration of the Z pulse. After twice the i SWAP time $\Delta t = h/2\gamma$, the system returns to the initial state $|11\rangle$ but with a minus sign. If the system starts in $|00\rangle$, $|01\rangle$, or $|10\rangle$, the state does not change since it is off-resonance with both avoided-level

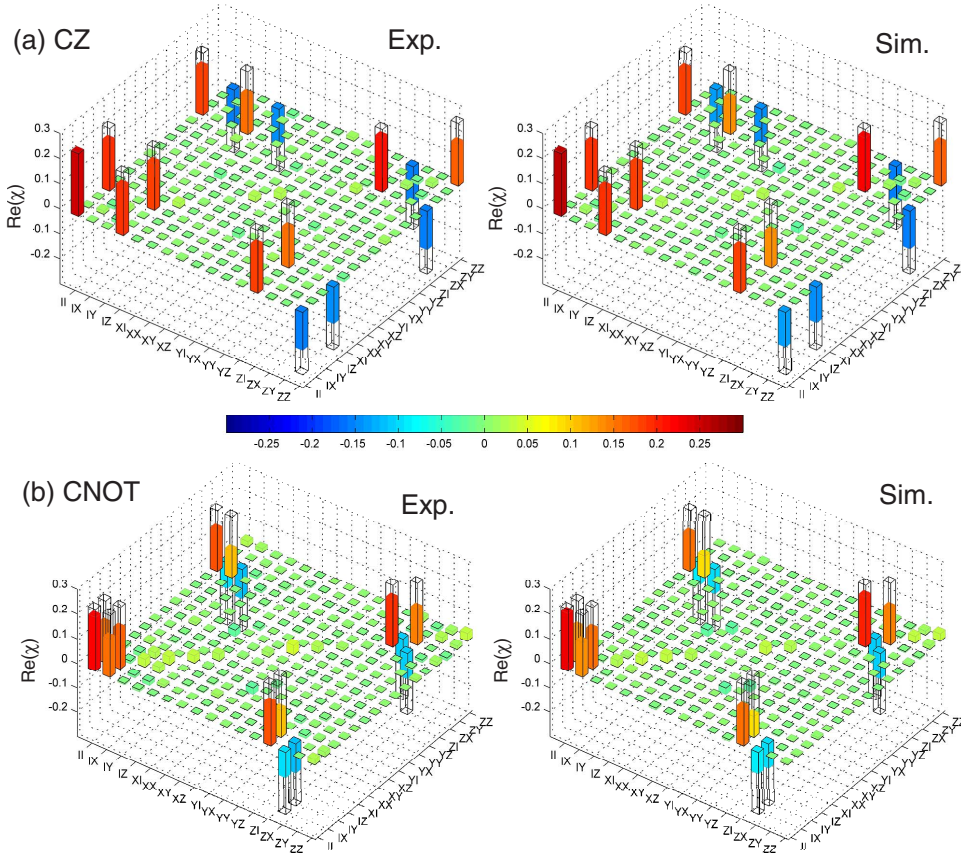


FIG. 4. (Color online) χ matrices of CZ and CNOT gates. (a) Left panel: the real part of the experimentally obtained χ matrix (χ_p) for the CZ gate with $F_p=0.70$. Right panel: the real part of the simulated χ matrix for the CZ gate with $F_p=0.67$. (b) Left panel: the real part of the simulated χ matrix for the CNOT gate with $F_p=0.56$. Right panel: the real part of the simulated χ matrix for the CNOT gate with $F_p=0.52$. The open boxes in the figure represent the ideal χ matrix.

crossings. A similar scheme using an adiabatic Z pulse has been used to successfully demonstrate a quantum algorithm³ and the same (nonadiabatic) scheme has recently been used to create a three-qubit entangled state in transmon qubits.⁵

To experimentally determine the amplitude and length of the required nonadiabatic Z pulse, we directly measured the coherent oscillation between the $|11\rangle$ and $|02\rangle$ states. This $(i\text{SWAP})^2$ operation sequence is shown in Fig. 3(a): we first prepare the $|11\rangle$ state with a π pulse to both qubits and then apply a Z pulse with amplitude Δi and length Δt to qubit B. Here only qubit B is probed and we adjust the measurement pulse amplitude so that the qubit is detected only when in the $|2\rangle$ (or higher) state.²⁵ In Fig. 3(b), we plot the tunneling probability $P_{|2\rangle}$ as a function of Δt and Δi , which shows the expected chevron pattern. The minimum oscillation frequency occurs at a value of Δi that agrees with i_0 determined in Fig. 2(a). The oscillation period $t_0=51.8$ ns is also consistent with the splitting size of the avoided crossing. At the intersection of these two dashed lines, the time evolution of the state produces a minus sign, as required for the CZ gate. We stress that no discernable increase in $P_{|2\rangle}$ is observed ($<1\%$) at this operation point $(\Delta t, \Delta i)=(t_0, i_0)$, confirming that we return to the $|11\rangle$ state after the CZ operation.

Because the qubits themselves also accumulate phase ϕ during the CZ pulse, the general unitary evolution from the gate is given by

$$U = \begin{pmatrix} 1 & 0 & 0 & 0 \\ 0 & e^{i\phi_A} & 0 & 0 \\ 0 & 0 & e^{i\phi_B} & 0 \\ 0 & 0 & 0 & -e^{i(\phi_A+\phi_B)} \end{pmatrix}. \quad (1)$$

By adding additional Z pulses to both qubits, we can compensate these phases and even place the minus sign at any diagonal position in the matrix.³ The compensation pulses are shown in Fig. 3(c), which consist of a fixed 10 ns pulse of variable amplitude i_{cmp} after the CZ pulse. In Fig. 3(d), we plot the tunneling probability of qubit B as a function of i_{cmp}^B for fixed i_{cmp}^A . The phase of qubit B is measured through a Ramsey fringe experiment. The (red) solid and (blue) dashed curves correspond to qubit A being in the $|0\rangle$ or $|1\rangle$ state. They both show a sinusoidal dependence on i_{cmp}^B , but are shifted by π from each other, confirming the correct operation of the CZ gate. A similar experiment was done for qubit A (data not shown).

The phases for the CZ gate are set by taking the values of i_{cmp} that give maximum probability when the control qubit is in the $|0\rangle$ state, as indicated by the vertical dashed-dotted line in Fig. 3(d). Controlled-NOT (CNOT) gates are constructed by combining the CZ gate with single-qubit rotations $U_{\text{CNOT}}=(I \otimes R_y^{\pi/2})\text{CZ}(I \otimes R_y^{-\pi/2})$, where R_y^θ represents the rotation of a single-qubit state by an angle θ about the y axis and I is the identity operator.

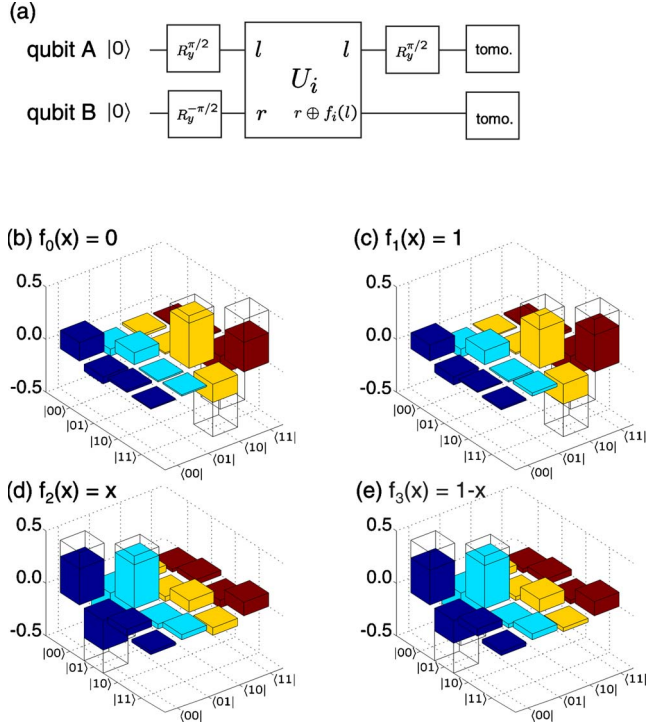


FIG. 5. (Color online) (a) Pulse sequence for the Deutsch-Jozsa algorithm. [(b)–(d)] Real part of the density matrix of the final state for four Deutsch-Jozsa functions. Open boxes represent the ideal density matrix.

C. Quantum process tomography

We evaluate the performance of these gates with QPT in which we determine the χ matrix with the elements defined as⁶

$$\mathcal{E}(\rho) = \sum_{m,n}^{16} E_m \rho E_n^\dagger \chi_{mn}. \quad (2)$$

Here, $\mathcal{E}(\rho)$ is the density matrix obtained by applying the gate to ρ and E_m 's are the operator bases formed by the Kronecker product of Pauli operators $\{I, \sigma_x, -i\sigma_y, \sigma_z\}$ for each qubit. For QPT, we prepare 16 input states in total, chosen from the set $\{|0\rangle, |1\rangle, |0\rangle + |1\rangle, |0\rangle + i|1\rangle\}$ for each qubit. After preparing these input states, we determine the density matrix of the output state with quantum state tomography¹⁶ (QST) in which we measure each qubit along

the six directions $\pm x$, $\pm y$, and $\pm z$ of the Bloch sphere.²⁶ For each combination of QPT and QST pulses, we repeat the sequence 1800 times to obtain the joint qubit probabilities $P_{AB} = P_{00}, P_{10}, P_{01},$ and P_{11} . After correcting for small measurement errors,¹⁵ we reconstruct the 16×16 experimental χ_e matrix from the resulting 16 density matrices.⁶ We assumed that input states are ideally prepared.²⁷ With experimental noise, the χ_e matrix found in this way is not necessarily physical, i.e., completely positive and trace preserving. We thus use convex optimization to obtain the physical matrix χ_p that best approximates χ_e , as used in Ref. 15. The difference between χ_e and χ_p is small as shown in Appendix B.

We plot the real part of χ_p for the CZ and CNOT gates in the left panel of Figs. 4(a) and 4(b). The open boxes represent the ideal χ matrix. The imaginary parts of χ_p have very small magnitude (<0.04 for CZ and <0.03 for CNOT) and are shown in Appendix C. For both gates, we observe elements with large amplitudes at the proper positions. More quantitative evaluation is obtained by calculating the process fidelity F_p , defined by $F_p = \text{Tr}(\chi_i \chi_p)$, where χ_i represents an ideal χ matrix. We obtain $F_p = 0.70$ for the experimentally measured CZ gate and 0.56 for the CNOT gate. For CZ gates with a minus sign at other positions on the diagonal, the measured F_p 's are 0.68, 0.69, and 0.70 for CZ₀₀, CZ₀₁, and CZ₁₀ (see Appendix C).

To understand the loss of process fidelity, we performed numerical simulations. We solved the standard master equation, $\dot{\rho} = -(i/\hbar)[\mathcal{H}, \rho] + \mathcal{L}[\rho]$, where \mathcal{H} is a 9×9 Hamiltonian for capacitively coupled phase qubits under rotating wave approximation and $\mathcal{L}[\rho] = \sum_{i=A,B} \sum_{j=1,2} \mathcal{L}_j^i \rho \mathcal{L}_j^{i\dagger} - \frac{1}{2} \mathcal{L}_j^{i\dagger} \mathcal{L}_j^i \rho - \frac{1}{2} \rho \mathcal{L}_j^{i\dagger} \mathcal{L}_j^i$. Here, for example, $\mathcal{L}_1^A = a_A / \sqrt{T_1^A}$ and $\mathcal{L}_2^A = a_A^2 / \sqrt{2} T_2^A$ describe the relaxation and dephasing for qubit A, respectively.²⁸ The entire sequence, including the QPT and QST pulses, was simulated to construct χ_{sim} . Experimental Ramsey interference shows Gaussian decay, which is not reproduced by the above master equation. Thus, in order to approximate this situation, we used an effective T_2 that depends on the length of the control sequence for a particular experiment t_{seq} . In particular, we used $T_2 = T_2^{\text{Ramsey}^2} / t_{\text{seq}}$ in the simulation in order for both the Gaussian decay and exponential decay to give the same decay factor at t_{seq} . The real part of χ_{sim} is shown in Fig. 4. The actual t_{seq} is 101.8 ns in QPT for CZ gates and 141.8 ns for CNOT gate. The simulation reproduces reasonably well the reduction in the expected elements and the appearance of

TABLE I. Summary of performance for Deutsch-Jozsa algorithm. Deutsch-Jozsa functions are defined as $f_0(x) = 0$, $f_1(x) = 1$, $f_2(x) = x$, and $f_3(x) = 1 - x$.

		Deutsch-Jozsa function			
		Constant		Balanced	
Element		f_0	f_1	f_2	f_3
$\langle 00 \rho 00\rangle + \langle 01 \rho 01\rangle$	Ideal	0	0	1	1
	Measured	0.29	0.28	0.76	0.74
$\langle 10 \rho 10\rangle + \langle 11 \rho 11\rangle$	Ideal	1	1	0	0
	Measured	0.71	0.72	0.24	0.26

small unwanted elements. These imperfections are removed as we increase the single-qubit coherence time in the simulation, which suggests that loss of F_p in our system is mostly dominated by single-qubit decoherence.²⁹ We note that it is possible to obtain more information on the decoherence mechanisms by analyzing the magnitude of particular elements in the χ matrix.³⁰ The simulated χ matrix of all CZ and CNOT gates including the imaginary parts are shown in Appendix D.

D. Deutsch-Jozsa algorithm

By using these conditional gates, we can perform the Deutsch-Jozsa algorithm⁶ using the pulse sequence described in Ref. 3. Figure 5(a) shows the pulse sequence for the Deutsch-Jozsa algorithm. The four different two-qubit gates U_i correspond to the four Deutsch-Jozsa functions, which we want to determine by a single-quantum evaluation of the function. They are given by

$$\begin{aligned} U_0 &= I \otimes I, \\ U_1 &= I \otimes R_x^\pi, \\ U_2 &= (I \otimes R_y^{\pi/2} R_x^\pi) CZ_{00} (I \otimes R_y^{\pi/2}), \\ U_3 &= (I \otimes R_y^{-\pi/2} R_x^\pi) CZ_{11} (I \otimes R_y^{-\pi/2}). \end{aligned} \quad (3)$$

The sequence is same as that used in Ref. 3 except that $R_y^{\pi/2}$ pulse was not applied to qubit B before the tomography. This makes the final state a superposition state. Also, in order to shorten the total sequence time, the last $R_y^{\pi/2}$ on qubit A was applied before the U_i part finishes. The real part of the final density matrices are plotted in Figs. 5(b)–5(e). The experimental probability to obtain the correct answer is summarized in Table I. Because our phase qubit has single-shot readout, we can obtain the correct answer to a single function query more than 70% of the time, greater than the 50% probability for a classical query and guess. We stress that no calibration for the measurement error is applied here.

IV. CONCLUSIONS

In conclusion, we have demonstrated CZ and CNOT gates in capacitively coupled phase qubits using the higher energy $|2\rangle$ state. Quantum process tomography measures a χ matrix that is in good accord with predictions, which is a definitive test of proper gate operation for any input state.

ACKNOWLEDGMENTS

The authors would like to thank F. K. Wilhelm and A. N. Korotkov for valuable discussion. They would also like to thank Y. Nakamura for useful comments on the manuscript. Semidefinite programming convex optimization was carried out using the open-source MATLAB packages YALMIP and SeDuMi. This work was supported by IARPA under ARO, Award No. W911NF-04-1-0204.

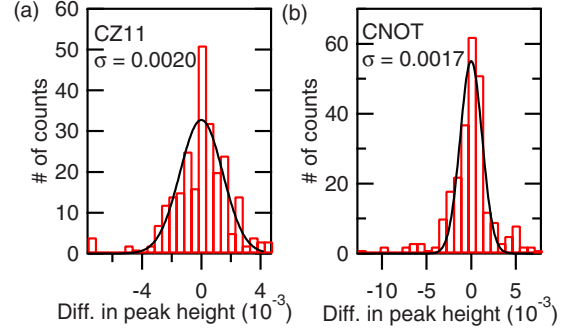


FIG. 6. (Color online) Histogram of the differences in the peak height of each of the 256 matrix elements in the real part of χ matrix. Data is for (a) CZ and (b) CNOT. The solid curves are a Gaussian fit to the data.

APPENDIX A: CALCULATION OF THE ENERGY BANDS AND TRANSITION MATRIX ELEMENTS

We calculated the energy band of the capacitively coupled flux-biased phase qubits by diagonalizing the following 9×9 Hamiltonian.^{22,23}

$$\begin{aligned} \mathcal{H} &\approx \begin{pmatrix} 0 & & & \\ & hf_{10}^{(A)} & & \\ & & hf_{10}^{(A)} + hf_{21}^{(A)} & \\ & & & \end{pmatrix} \otimes I_2 + I_1 \\ &\otimes \begin{pmatrix} 0 & & & \\ & hf_{10}^{(B)} & & \\ & & hf_{10}^{(B)} + hf_{21}^{(B)} & \\ & & & \end{pmatrix} - g \begin{pmatrix} 0 & -1 & 0 \\ 1 & 0 & -\sqrt{2} \\ 0 & \sqrt{2} & 0 \end{pmatrix} \\ &\otimes \begin{pmatrix} 0 & -1 & 0 \\ 1 & 0 & -\sqrt{2} \\ 0 & \sqrt{2} & 0 \end{pmatrix}, \end{aligned} \quad (A1)$$

where $f_{i,j}^{(A)}$ ($f_{i,j}^{(B)}$) is the flux-dependent transition frequency between i th and j th state of the qubit A (B) and g is the coupling energy between the qubits. The last term in the Hamiltonian is based on $\sigma_y \sigma_y$ -type coupling of the two qubits. To calculate the transition matrix from the ground state $|g\rangle$ to the excited state $|e\rangle$ in the spectroscopy experiment, we calculated the transition matrix element of $|\langle e|a^\dagger + a|g\rangle|^2$ for one-photon excitation and $|\sum_i \frac{\langle e|a^\dagger + a|i\rangle \langle i|a^\dagger + a|g\rangle}{E_e - E_i - hf_d}|^2$ for two-photon excitation,³¹ where $a(a^\dagger)$ is an annihilation (creation) operator for the harmonic oscillator, E_i is the energy gap of the state $|i\rangle$ from the ground state, and f_d is the frequency of the μ -wave drive, which is set to be $E_e/2h$ in the calculation.

APPENDIX B: DIFFERENCE BETWEEN χ_p AND χ_e

We checked the difference between χ_e (the experimental χ matrix) and χ_p (the physical χ matrix) by histogramming the differences in the peak height $\Delta = \chi_e - \chi_p$ of each of the 256 matrix elements in the real part.¹⁰ We fit it by Gaussian $a \exp(-\Delta^2/\sigma^2)$ as shown in Fig. 6. The obtained σ are 0.0020 for CP₁₁ and 0.0017 for CNOT gate, which implies χ_e and χ_p are close.

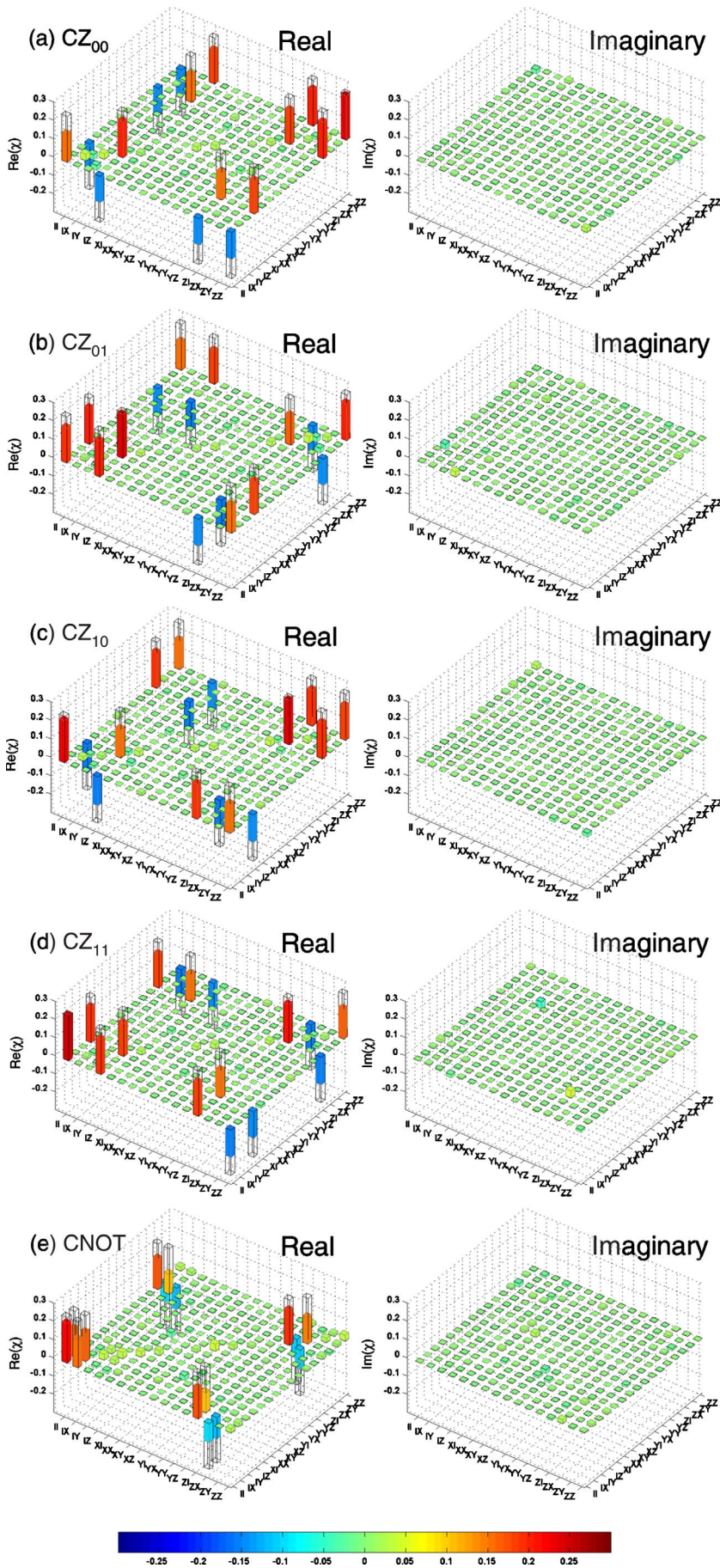


FIG. 7. (Color online) χ_p of (a) CZ_{00} , (b) CZ_{01} , (c) CZ_{10} , (d) CZ_{11} , and (e) CNOT. Process fidelity F_p are 0.68, 0.69, 0.70, 0.70, and 0.56, respectively.

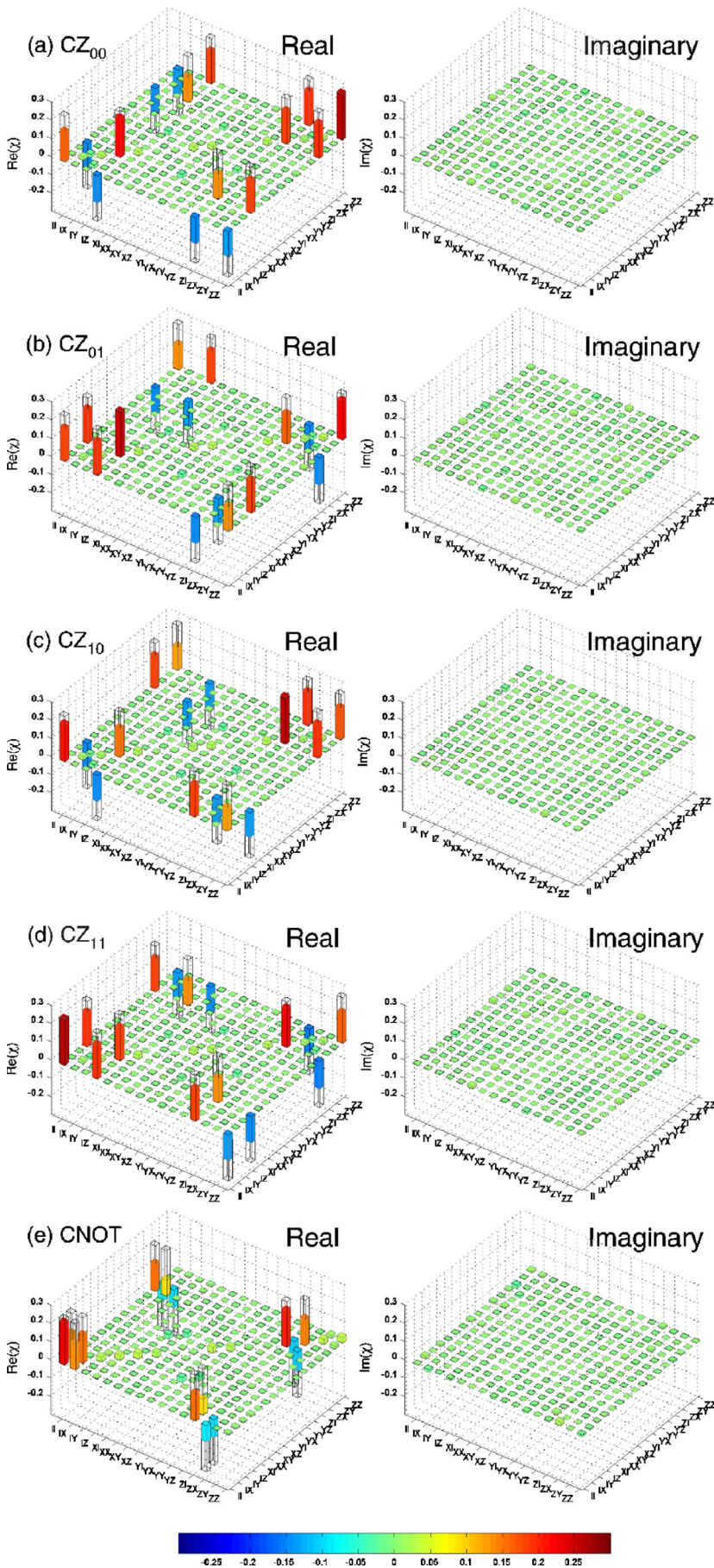


FIG. 8. (Color online) Simulated χ matrix of (a) CZ_{00} , (b) CZ_{01} , (c) CZ_{10} , (d) CZ , and (e) CNOT. Process fidelity F_p are 0.67, 0.67, 0.66, 0.67, and 0.52, respectively.

APPENDIX C: χ MATRIX FOR ALL GATES

In Fig. 7, the physical χ matrix χ_p is plotted for all the CZ and CNOT gates.

APPENDIX D: SIMULATED χ MATRIX FOR ALL GATES

In Fig. 8, the simulated χ matrix is plotted for all CZ and CNOT gates.

*anc@physics.ucsb.edu

†martinis@physics.ucsb.edu

- ¹T. D. Ladd, F. Jelezko, R. Laflamme, Y. Nakamura, C. Monroe, and J. L. O'Brien, *Nature (London)* **464**, 45 (2010).
- ²J. Clarke and F. K. Wilhelm, *Nature (London)* **453**, 1031 (2008).
- ³L. DiCarlo, J. M. Chow, J. M. Gambetta, L. S. Bishop, B. R. Johnson, D. I. Shuster, J. Majer, A. Blais, L. Frunzio, S. M. Girvin, and R. J. Schoelkopf, *Nature (London)* **460**, 240 (2009).
- ⁴M. Neeley, R. C. Bialczak, M. Lenander, E. Lucero, M. Mariantoni, A. D. O'Connell, D. Sank, H. Wang, M. Weides, J. Wenner, Y. Yin, T. Yamamoto, A. N. Cleland, and J. M. Martinis, *Nature (London)* **467**, 570 (2010).
- ⁵L. DiCarlo, M. D. Reed, L. Sun, B. R. Johnson, J. M. Chow, J. M. Gambetta, L. Frunzio, S. M. Girvin, M. H. Devoret, and R. J. Schoelkopf, *Nature (London)* **467**, 574 (2010).
- ⁶M. A. Nielsen and I. L. Chuang, *Quantum Computation and Quantum Information* (Cambridge University Press, Cambridge, England, 2000).
- ⁷T. Yamamoto, Y. A. Pashkin, O. Astafiev, Y. Nakamura, and J. S. Tsai, *Nature (London)* **425**, 941 (2003).
- ⁸J. H. Plantenberg, P. C. de Groot, C. J. P. M. Harmans, and J. E. Mooij, *Nature (London)* **447**, 836 (2007).
- ⁹A. M. Childs, I. L. Chuang, and D. W. Leung, *Phys. Rev. A* **64**, 012314 (2001).
- ¹⁰J. L. O'Brien, G. J. Pryde, A. Gilchrist, D. F. V. James, N. K. Langford, T. C. Ralph, and A. G. White, *Phys. Rev. Lett.* **93**, 080502 (2004).
- ¹¹N. K. Langford, T. J. Weinhold, R. Prevedel, K. J. Resch, A. Gilchrist, J. L. O'Brien, G. J. Pryde, and A. G. White, *Phys. Rev. Lett.* **95**, 210504 (2005).
- ¹²N. Kiesel, C. Schmid, U. Weber, R. Ursin, and H. Weinfurter, *Phys. Rev. Lett.* **95**, 210505 (2005).
- ¹³M. Riebe, K. Kim, P. Schindler, T. Monz, P. O. Schmidt, T. K. Körber, W. Hänsel, H. Häffner, C. F. Roos, and R. Blatt, *Phys. Rev. Lett.* **97**, 220407 (2006).
- ¹⁴T. Monz, K. Kim, W. Hänsel, M. Riebe, A. S. Villar, P. Schindler, M. Chwalla, M. Hennrich, and R. Blatt, *Phys. Rev. Lett.* **102**, 040501 (2009).
- ¹⁵R. C. Bialczak, M. Ansmann, M. Hofheinz, E. Lucero, M. Neeley, A. D. O'Connell, D. Sank, H. Wang, J. Wenner, M. Steffen, A. N. Cleland, and J. M. Martinis, *Nat. Phys.* **6**, 409 (2010).
- ¹⁶M. Steffen, M. Ansmann, R. C. Bialczak, N. Katz, E. Lucero, R. McDermott, M. Neeley, E. M. Weig, A. N. Cleland, and J. M. Martinis, *Science* **313**, 1423 (2006).
- ¹⁷F. Motzoi, J. M. Gambetta, P. Rebentrost, and F. K. Wilhelm, *Phys. Rev. Lett.* **103**, 110501 (2009).
- ¹⁸E. Lucero, J. Kelly, R. C. Bialczak, M. Lenander, M. Mariantoni, M. Neeley, A. D. O'Connell, D. Sank, H. Wang, M. Weides, J. Wenner, T. Yamamoto, A. N. Cleland, and J. M. Martinis, *Phys. Rev. A* **82**, 042339 (2010).
- ¹⁹E. Lucero, M. Hofheinz, M. Ansmann, R. C. Bialczak, N. Katz, M. Neeley, A. D. O'Connell, H. Wang, A. N. Cleland, and J. M. Martinis, *Phys. Rev. Lett.* **100**, 247001 (2008).
- ²⁰R. C. Bialczak, R. McDermott, M. Ansmann, M. Hofheinz, N. Katz, E. Lucero, M. Neeley, A. D. O'Connell, H. Wang, A. N. Cleland, and J. M. Martinis, *Phys. Rev. Lett.* **99**, 187006 (2007).
- ²¹P. Bushev, C. Müller, J. Lisenfeld, J. Cole, A. Lukashenko, A. Shnirman, and A. Ustinov, *Phys. Rev. B* **82**, 134530 (2010).
- ²²M. Steffen, J. M. Martinis, and I. L. Chuang, *Phys. Rev. B* **68**, 224518 (2003).
- ²³A. G. Kofman, Q. Zhang, J. M. Martinis, and A. N. Korotkov, *Phys. Rev. B* **75**, 014524 (2007).
- ²⁴F. W. Strauch, P. R. Johnson, A. J. Dragt, C. J. Lobb, J. R. Anderson, and F. C. Wellstood, *Phys. Rev. Lett.* **91**, 167005 (2003).
- ²⁵M. Neeley, M. Ansmann, R. C. Bialczak, M. Hofheinz, E. Lucero, A. D. O'Connell, D. Sank, H. Wang, J. Wenner, A. N. Cleland, M. R. Geller, and J. M. Martinis, *Science* **325**, 722 (2009).
- ²⁶M. Neeley, M. Ansmann, R. C. Bialczak, M. Hofheinz, E. Lucero, A. D. O'Connell, D. Sank, H. Wang, J. Wenner, A. N. Cleland, M. R. Geller, and J. M. Martinis, *Nat. Phys.* **4**, 523 (2008).
- ²⁷For identity operation, namely, QST right after the preparation pulses, we obtained F_p of 0.91.
- ²⁸D. F. Walls and G. J. Milburn, *Phys. Rev. A* **31**, 2403 (1985).
- ²⁹According to the simulation, roughly half of the fidelity loss is caused by pure dephasing (T_2) both in CZ and CNOT gates.
- ³⁰A. G. Kofman and A. N. Korotkov, *Phys. Rev. A* **80**, 042103 (2009).
- ³¹C. Cohen-Tannoudji, J. Dupont-Roc, and G. Grynberg, *Atom-Photon Interaction* (Wiley, New York, 1992) Chap. IIIC.